Seismic evidence for widespread crustal flow caused by extension in the western USA

M.P. Moschetti[1†], M.H. Ritzwoller[1], and F. Lin[1]

1 - Center for Imaging the Earth's Interior, Department of Physics, University of Colorado at Boulder, Campus Box 390, Boulder, CO 80309, USA

† To whom correspondence should be directed: morganm@ciei.colorado.edu, 303-735-3048

Updated for submission: November 23, 2008.

ABSTRACT

Seismic anisotropy is a powerful indicator of deformation and flow within Earth's interior. Observations of short period ($<$ 20 sec) surface wave dispersion constrain anisotropy, but difficulties in obtaining such measurements have inhibited studies in the western USA. Seismic ambient noise tomography and its application to data from the EarthScope/USArray provide the means to infer crustal radial anisotropy unambiguously. To fit the Rayleigh and Love wave dispersion curves simultaneously in the principal extensional provinces of the western USA requires the introduction of middle to lower crustal radial anisotropy. This anisotropy probably results from the lattice preferred orientation of crustal minerals and is consistent with widespread lateral crustal flow in response to Cenozoic extension in the western USA.

MANUSCRIPT

Studies in the laboratory have shown that many earth materials are strongly anisotropic (*1*). Both azimuthal (*2-4*) and radial (*5,6*) anisotropy have been observed clearly at large-scales in the upper mantle, presumably due to the lattice-preferred orientation (LPO) of olivine caused by shear strains that have accumulated as a result of plate motions. Observations of crustal anisotropy at large scales are much more rare and less robust, but are needed to improve understanding of the deformation and flow patterns within the crust that result from tectonic processes. To infer information about crustal anisotropy requires surface wave dispersion measurements at periods below 20 sec, but waves at these periods are strongly scattered and attenuated as they propagate from distant earthquakes. Only regions with very thick crust, therefore, have been amenable to surface wave inversions for crustal anisotropy. For example, Shapiro et al. observed crustal radial anisotropy and inferred middle crustal flow beneath the Tibetan Plateau (*7*). The inference of the 3D distribution of anisotropy in regions with normal to thin continental crust is now possible, however, from surface wave studies based on ambient seismic noise (*8,9*). Ambient noise tomography (ANT) produces surface wave dispersion measurements down to periods below 10 sec. The application of ANT to data from the Transportable Array (TA) component of the EarthScope/USArray generates high resolution images of isotropic S-wave speeds in the crust and uppermost mantle across the western USA (*10*). Here, for the first time, we show similarly high resolution images of the radial anisotropy of the crust and uppermost mantle in the western USA and discuss implications for crustal flow.

We follow the ambient noise data processing protocol of Bensen et al. (*11*) to obtain cross-correlations between long time series (up to several years) of ambient noise recorded at pairs of seismic stations. The cross-correlations provide three-component, inter-station "empirical Green's functions" on which Rayleigh and Love wave group and phase speeds measurements are obtained at periods from 6 to 40 sec (*12,13*). These measurements are strongly sensitive to S-wave speeds in the crust and uppermost mantle, and the short period band facilitates the imaging of structures shallower than can be resolved using teleseismic earthquake observations alone (*14*). At each point in time, the TA comprises about 400 broadband stations on a 70 km grid (Fig. 1A). We processed waveforms from 526 TA stations acquired between October 2004 through December 2007 obtaining Rayleigh and Love wave dispersion measurements along more than 120,000 inter-station paths. This results in unprecedented path density and resolution (Fig. S1) across the western USA (*12,13*). Estimation of measurement errors is described in the Supplementary Materials. Love wave group speed measurements are less reliable than the other measurements, and we retain only measurements of Rayleigh wave group (RG) and phase speeds (RP) and Love wave phase speeds (LP) in the following bands: RG, 6-40 sec; RP, 6-40 sec; LP, 8-32 sec. The inversion of the dispersion measurements initiates with the construction of dispersion maps (e.g., Fig. 1B,C,D). A traditional straight ray tomographic method is used to produce the dispersion maps (*15*). Uncertainty estimates, however, are based on the eikonal tomography method (*16*) as described in the Supplementary Materials (Fig. S2). Estimated uncertainties in the dispersion maps vary with period, measurement type (Rayleigh phase, Rayleigh group, Love phase), and location.

We present results of inversions for radial anisotropy (transverse isotropy with a radial symmetry axis) in the crust and uppermost mantle underlying the western USA. The generation of radial anisotropy by LPO depends on the preferential vertical alignment of mineral slow axes and does not preclude preferred azimuthal crystalline orientations. Radial anisotropy may also be produced by microcracks, but microcracks are expected to be closed in the deep crust due to high lithostatic pressures. Radial anisotropy manifests itself as the difference in the speeds of horizontally- and vertically-polarized shear waves (V_{SH} and V_{SV}, respectively), and is, therefore, sometimes referred to as polarization anisotropy. Radial anisotropy is inferred by simultaneously interpreting the dispersion characteristics of Rayleigh and Love waves, which depend predominantly on V_{SV} and V_{SH}, respectively. In particular, radial anisotropy can be inferred from the "Rayleigh - Love discrepancy", which is a measure of the misfit to the Rayleigh and Love wave dispersion curves that results from a best fitting isotropic model ($V_S = V_{SH} = V_{SV}$).

To illustrate the existence and nature of the Rayleigh-Love discrepancy in the western USA and to localize its source, we present three inversions. Inversion I defines a purely isotropic reference state in which there is a single shear wave speed at each depth in the crust and upper mantle. Inversion II is a perturbation to the isotropic reference, permitting radial anisotropy in the upper mantle but not the crust. Inversion III further perturbs the model by allowing radial anisotropy in the crust with an additional perturbation in the upper mantle. In each case, the data are the same: local dispersion curves with uncertainties that are constructed from the dispersion maps on a 0.5°-by-0.5° grid across the study region (e.g., Fig. 2A for a point in central Nevada).

In Inversion I, the isotropic model is parameterized with four crustal layers (a sedimentary layer and three underlying crystalline layers) and five cubic B-splines in the mantle. We require crustal shear-velocities to increase monotonically with depth except within the Cascadia forearc region (outlined with a dashed box in Figure 1A), where the Rayleigh wave data require non-monotonic shear wave speeds. We impose a layer thickness ratio of 1:2:2 for the three crystalline crustal layers. Receiver function estimates provide initial constraints on crustal thicknesses (*17*). At each grid point we use a Monte-Carlo method to construct a set of models that fit the dispersion curves within a threshold defined as twice the chi-squared misfit of the best-fitting model. Forward modeling is performed with the MINEOS (*18*) code and model space sampling is performed with the Neighbourhood Algorithm (*19*). An example best-fitting model for a point in central Nevada from Inversion I is shown in Figure 2B. The range of acceptable models for this point is shown in the Supplementary Materials (Fig. S3A, B).

Inversion I produces a large Rayleigh-Love discrepancy across most of the western USA, presented in Figure 2C as "reduced" chi-squared misfit, $\chi^2 = n^{-1} \sum_{i=1}^{n} \sigma_i^{-2}(d_i - p_i)^2$, referred to hereafter as chi-squared. Here, n is the number of discrete dispersion measurements, d_i, p_i are the predicted dispersion values from a trial model, and σ_i are the measurement errors (discussed in the Supporting Online Materials). The average chi-squared from the best fitting model across the region from Inversion I is $\chi_I^2 = 10.6$. At locations with a large chi-squared value (e.g., central Nevada, Fig. 1A), Love wave phase speeds computed from the isotropic model under-predict the observed speeds above about 15 sec period, whereas the Rayleigh wave phase and group speeds are slightly over-predicted between 20 and 30 sec period and severely over-predicted below 20 sec. Because more than twice the number of Rayleigh than Love wave measurements are inverted, the isotropic model tends to fit the Rayleigh wave data better than the Love wave data.

Inversion II attempts to resolve this Rayleigh-Love discrepancy by introducing a constant radial anisotropy in the upper mantle. We permit radial anisotropy with an amplitude ($2\left|V_{SH}-V_{SV}\right|/(V_{SH}+V_{SV})$) of up to 10%, consistent with the largest values observed by Nettles and Dziewonski (*20*). The introduction of mantle anisotropy (e.g., Fig. 2E) improves data fit significantly (Fig. 2D,F) compared with the isotropic model, reducing overall $\chi^2_{II} = 5.36$, a 47% variance reduction. Regions of relatively poor data fit persist, however. Residual misfit to the Rayleigh wave phase and group speeds is largest at periods less than about 15 and 20 sec period, respectively, whereas misfit to the Love wave phase speeds remains largest between about 15 and 25 sec period (e.g., Fig. 2D). The amplitude of radial anisotropy in the mantle that results from this inversion is shown in Figure S4.

Further reduction in the Rayleigh-Love discrepancy requires the introduction of radial anisotropy in the crust. In Inversion III, we perturb the best fitting model from Inversion II by allowing a constant anisotropic perturbation to middle and lower crustal shear wave speeds and an additional perturbation to mantle anisotropy. This inversion exhibits a trade-off between the amplitude of radial anisotropy in the crust and mantle, with the resulting amplitude of crustal and mantle anisotropy negatively correlating across all tectonic regions, reflected as a negative slope of the misfit ellipses shown in Figure 3. In some regions (e.g., Sierra Nevada, much of the Colorado Plateau; Fig. 3B,C) radial anisotropy is not required in either the crust or mantle to fit the data and in other regions (e.g., central Oregon; Fig. 3A) it is required in either the crust or mantle. But, in extensional provinces within the western USA (e.g., Basin and Range, Rocky Mountain Basin and Range, and the Omineca Extended Belt), positive crustal anisotropy ($V_{SH} > V_{SV}$) (Fig. 3D,E,F) is required irrespective of the strength of mantle anisotropy. Although the amplitude of crustal anisotropy in these regions depends on the amplitude of the mantle anisotropy, the sign of the crustal radial anisotropy is unique and positive. We refer to the regions with clear positive crustal radial anisotropy as the anisotropic crustal regions. Outside of the anisotropic crustal regions, crustal anisotropy is not required by the data.

To construct a single model from Inversion III, we constrain upper mantle anisotropy to lie within 2% of the best-fitting model from Inversion II (Fig. S4). Because of the negative correlation between crustal and mantle anisotropy, this constraint will produce a conservative (lower bound) estimate of the amplitude of crustal anisotropy. Example results for Central Nevada are shown in Figures 4A,B. The mean amplitude of radial anisotropy ($2\,|V_{SH} - V_{SV}|\,/(V_{SH} + V_{SV})$) in the crust and mantle across the anisotropic crustal regions are 3.6% and 5.3%, respectively. Only positive anisotropy is observed ($V_{SH} > V_{SV}$). Misfit resulting from Inversion III is presented in Figure 4C, and mean chi-squared across the study region is $\chi^2_{III} = 1.74$, an 80% variance reduction compared to the isotropic model from Inversion I. The introduction of crustal radial anisotropy on average resolves the residual Rayleigh-Love discrepancy to $\chi^2 < 2$, on average, except in small discrete areas outside the anisotropic crustal regions where other near surface structural variables would need to be introduced to fit the data (e.g., Olympic Peninsula accretionary wedge, northern Central Valley of California, southern Salton Trough, southern Cascades, Yellowstone).

The amplitude of radial anisotropy in the crust and mantle of the best fitting model from Inversion III is shown in Figures 4D and 4E, respectively. The resulting patterns of strong crustal radial anisotropy strongly correlate with the predominant extensional provinces in the region. Cenozoic (since about 66 Ma) extension in the western USA has been primarily confined to the Basin and Range (BR), the Rocky Mountains Basin and Range (RMBR), and the Omineca extended belt (OEB) provinces (Fig. 1A) (*21*). Average extension across these provinces has been estimated to range up to 100% (*21,22*). Strong crustal radial anisotropy is evident across nearly the entire BR province and terminates abruptly near its edges; e.g., along the Wasatch and Sierra Nevada ranges, along the Snake River Plain, and along the Colorado Plateau. Anisotropic amplitudes greater than 5% are present in all three extensional provinces. The largest continuous region of large amplitude anisotropy (>5%) occurs in central

Nevada. Observations of seismic anisotropy in the mantle are routinely ascribed to LPO development and used to infer characteristics about the mantle flow field (*23,24*). Because of the relative dearth of observations of middle to lower crustal anisotropy, such inferences are not as common.

Various studies suggest that the lower crust within such highly extended regions may flow laterally in response to extension (*25-27*). Heretofore, no direct evidence of regional-scale flow has been observed to support this hypothesis. We interpret the observed crustal radial anisotropy to result from the LPO of seismically anisotropic crustal minerals induced by flow along sub-horizontal planes in the middle and lower crust. These observations are consistent with the hypothesis that the extensional provinces of the western USA have experienced large-scale lateral crustal flow. At middle and lower crustal depths, micro-fractures are closed by lithostatic stresses and the LPO of micas and amphiboles significantly contributes to seismic anisotropy (*28-30*). An improved understanding of middle to lower crustal P-T conditions and composition in these regions is required to evaluate the contributions to observed anisotropy from specific minerals. Our results suggest, however, that the deep crustal response to extension in the western USA is widespread and relatively uniform.

Acknowledgments

This research was supported by NSF grants EAR-0450082 and EAR-0711526. M.P.M. acknowledges a National Defense Science and Engineering Graduate Fellowship from the American Society for Engineering Education. The facilities of the IRIS Data Management System, and specifically the IRIS Data Management Center, were used to access the waveform and metadata required in this study. The IRIS DMS is funded by the National Science Foundation and specifically the GEO Directorate through the Instrumentation and Facilities Program of the National Science Foundation under Cooperative Agreement EAR-0552316.

References and Notes

1. M. Takanashi, O. Nishizawa, K. Kanagawa, K. Yasunaga, *Geophys. J. Int.* **145**, 1 (2001).
2. J.-P. Montagner, T. Tanimoto, *J. Geophys. Res.* **96**, 20337–20351 (1991).
3. P. G. Silver, *Ann. Rev. Earth Planet. Sci* **24**, 385–421 (1996).
4. F. Marone, B. Romanowicz, *Nature* **447**, 198–201 (2007).
5. G. Ekström, A. M. Dziewonski, *Nature* **394**, 168–172 (1998).
6. N. M. Shapiro, M. H. Ritzwoller, *Geophys. J. Int.* **151**, 1 (2002).
7. N. M. Shapiro, M. H. Ritzwoller, P. H. Molnar, V. Levin, *Science* **305**, 233–236 (2004).
8. K. G. Sabra, P. Gerstoft, P. Roux, W.A. Kuperman, M. C. Fehler, *Geophys. Res. Lett.* **32**, 32 (2005).
9. N. M. Shapiro, M. Campillo, L. Stehly, M. H. Ritzwoller, *Science* **307**, 5715 (2005).
10. Y. Yang, M. H. Ritzwoller, F.-C. Lin, M. P. Moschetti, N. M. Shapiro *J. Geophys. Res. in press* (2008).
11. G. D. Bensen et al., *Geophys. J. Int.* **169**, 3 (2007).
12. M. P. Moschetti, M. H. Ritzwoller, N. M. Shapiro, *Geochem. Geophys. Geosys.* **8**, Q08010 (2007).
13. F. Lin, M. P. Moschetti, M. H. Ritzwoller, *Geophys. J. Int.* **173**, 1 (2008).
14. Y. Yang, M. H. Ritzwoller, *Geophys. Res. Lett.* **5**, L04308 (2008).

15. M. P. Barmin, M. H. Ritzwoller, A.L. Levshin, *Pure Appl. Geophys.*, **158**, 8 (2001).

16. F. Lin, M. H. Ritzwoller, R. Snieder, *Geophys. J. Int. submitted.*

17. H. J. Gilbert, M.J. Fouch, *Eos Trans. AGU* **88**, S41B-0558 (2007).

18. G. Masters, M. P. Barmin, S. Kientz, *California Institute of Technology* (2007).

19. M. Sambridge, *Geophys. J. Int.* **138**, 2 (1999).

20. M. Nettles, A. M. Dziewonski, *J. Geophys. Res.* **113**, B02303 (2008).

21. B. Wernicke, in *The Cordilleran Orogen: Conterminous US*, B. C. Burchfiel, P. W. Lipman, M. L. Zoback, Eds., (Geol. Soc. Amer., Boulder, CO, 1992), pp 553-581.

22. S. U. Janecke, *Geol. Soc. Amer., Abstracts with Programs* **36**, 5 (2004).

23. P. G. Silver, W. E. Holt, *Science*, **295**, 1054–1057 (2002).

24. T. W. Becker, V. Schulte-Pelkum, D. K. Blackman, J. B. Kelloff, R. J. O'Connell, *Earth Plan. Sci. Lett.* **247**, 235–251 (2006).

25. L. Block, L. H. Royden, *Tectonics* **9**, 4 (1990).

26. P. Bird, *J. Geophys. Res.* **96**, B6 (1991).

27. S. Kruse, M. McNutt, J. Phipps-Morgan, L. Royden, B. Wernicke, *J. Geophys. Res.* **96**, B3 (1991).

28. P. N. J. Rasolofosaon, W. Rabbel, S. Siegesmund, A. Vollbrecht, *Geophys. J. Int.* **141**, 2 (2000).

29. T. Weiss, S. Siegesmund, W. Rabbel, T. Bohlen, M. Pohl, *Pure Appl. Geophys* **156**, 97–122 (1999).

30. D. J. Tatham, G. E. Lloyd, R. W. H Butler, M. Casey, *Earth Plan. Sci. Lett.* **267**, 118–128 (2008).

241

Figure 1. (a) Map of the study region. Seismic stations predominantly from the EarthScope USArray/Transportable Array are plotted as black triangles. The major tectonic boundaries are drawn with black lines and the boundaries of the predominant extensional provinces are drawn with red lines, including the Basin and Range (BR), Omineca extended belt (OEB), and Rocky Mountain Basin and Range (RMBR). Inversion results presented in Figs. 2A,B,D,E and 4A,B are from the Basin and Range point (244.0, 40.0)
242 plotted with a white square. Anisotropy trade-off results presented in Figure 3 for points from the BR, Central Oregon (CtOR), Colorado Plateau (CP), OEB, RMBR and Sierra Nevada (SN) and are also plotted as white squares. The dashed rectangle in the Cascadia region defines the region where the vertical monotonicity constraint is not applied in the crust. (b) - (d) Example dispersion maps are presented for Rayleigh wave phase (RP) and group speeds (RG) and Love wave phase speeds (LP), respectively, at 20 sec period.

Figure 2. Results from Inversions I and II. (a) Example observed local Rayleigh (RP, RG) and Love wave (LP) dispersion curves (identified by 1-sigma error bars) compared with black curves predicted by the best-fitting isotropic model from Inversion I (Fig. 1B) at a grid point in the Basin and Range Province (BR white box, Fig. 1A). The misfit reflects the Rayleigh-Love discrepancy and identifies the need for radial anisotropy. (b) The best-fitting isotropic shear-velocity model from Inversion I at the Basin and Range point. (c) Reduced chi-squared misfit to the Rayleigh and Love wave dispersion curves
243 for the best-fitting model from Inversion I; average $\chi_I^2 = 10.6$. The 100 km resolution contour corresponding to the Rayleigh wave group speed 16 sec period map is plotted with a dashed black line. (d) Same as (a), but fit curves are for the best-fitting model from Inversion II which includes radial anisotropy in the mantle, $V_{SH} \neq V_{SV}$. (e) Same as (b), but the best fitting model is from Inversion II. (f) Same as (c), but misfit is for the best-fitting model from Inversion II; average $\chi_{II}^2 = 5.36$. The Rayleigh-Love discrepancy is resolved partially by introducing mantle anisotropy.

Figure 3. Misfit ellipses reflecting the trade-off between the amplitude of crustal and mantle anisotropy ($2(V_{SH} - V_{SV})/(V_{SH} + V_{SV})$) resulting from inversions with no constraints on the strength of anisotropy in the crust or mantle. Symbol colors correspond to the chi-squared misfit plotted at the corresponding location for the amplitude of crustal and mantle anisotropy: black symbols denote $1.5 \leq \chi^2 \leq 2.0$; blue denote $1.0 \leq \chi^2 < 1.5$;
244 and red are for $\chi^2 < 1.0$. Results are presented for the six regions identified with white boxes in Fig. 1A: (a) Central Oregon (CtOR), (b) Sierra Nevada (SN), (c) Colorado Plateau (CP), (d) Basin and Range (BR), (e) Rocky Mountain Basin and Range (RMBR), and (f) Omineca extended belt (OEB). The locations BR, RMBR and OEB fall within the principal extensional pronvinces of the western USA.

Figure 4. (a) Same as Figs. 2A,D, but fit curves are for the best-fitting model from Inversion III which includes radial anisotropy in the crust and upper mantle, $V_{SH} \neq V_{SV}$. (b) Same as Figs. 2B,E, but the best fitting model is from Inversion III. (c) Same as Figs. 2C,F, but misfit is for the best-fitting model from Inversion III; average $\chi^2_{III} = 1.74$. The Rayleigh-Love discrepancy is largely resolved by introducing crustal radial anisotropy on top of mantle anisotropy. The amplitudes of radial anisotropy $(2(V_{SH} - V_{SV})/(V_{SH} + V_{SV}))$ from Inversion III are presented in (d) for the crust and in (e) for the mantle. Extensional province boundaries are drawn with red lines. The 100 km resolution contour corresponding to the Rayleigh wave group speed 16 sec period map is plotted with a dashed black line (Fig. S1).

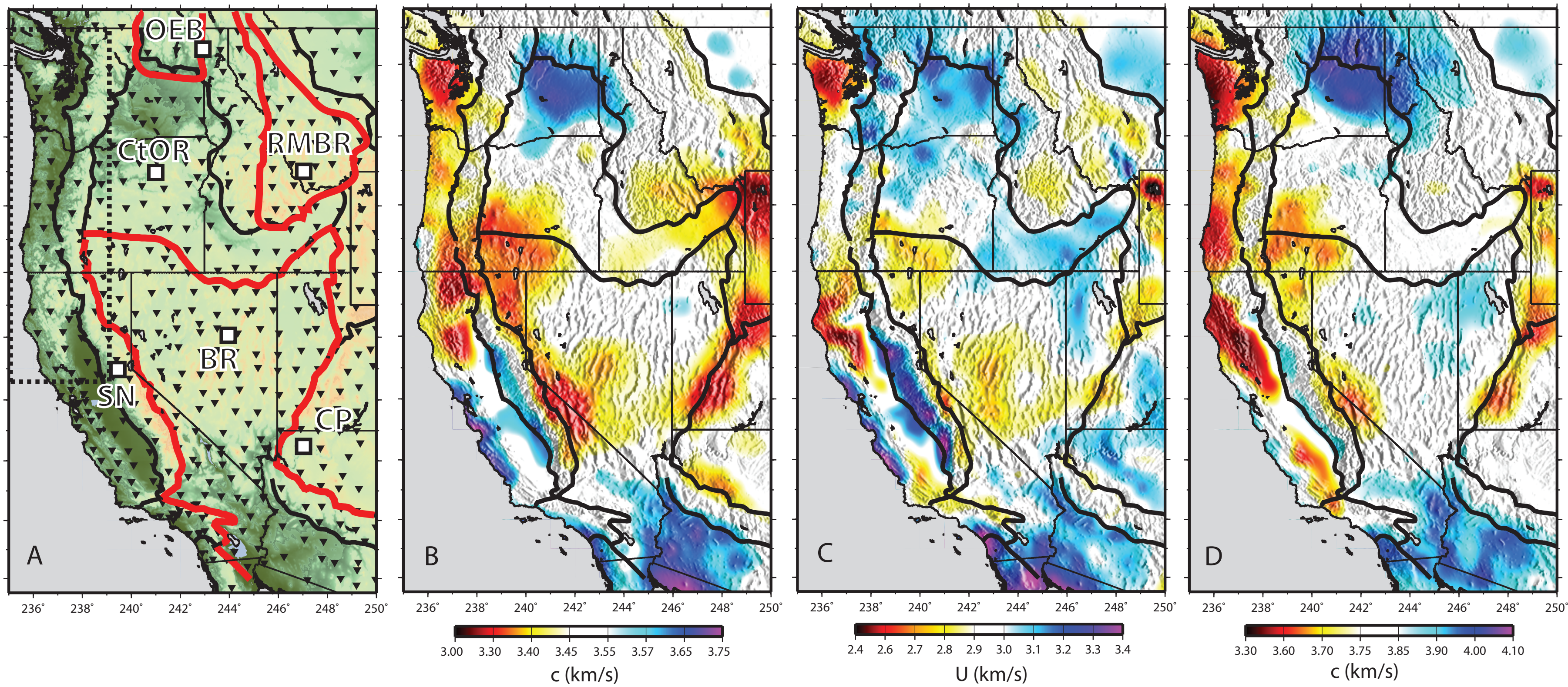
OEB
CtOR
RMBR
BR
SN
CP
A
B
C
D
48°
46°
44°
42°
40°
38°
36°
34°
32°
236° 238° 240° 242° 244° 246° 248° 250°
3.00 3.30 3.40 3.45 3.55 3.57 3.65 3.75
c (km/s)
2.4 2.6 2.7 2.8 2.9 3.0 3.1 3.2 3.3 3.4
U (km/s)
3.30 3.60 3.70 3.75 3.85 3.90 4.00 4.10
c (km/s)

Figure 1

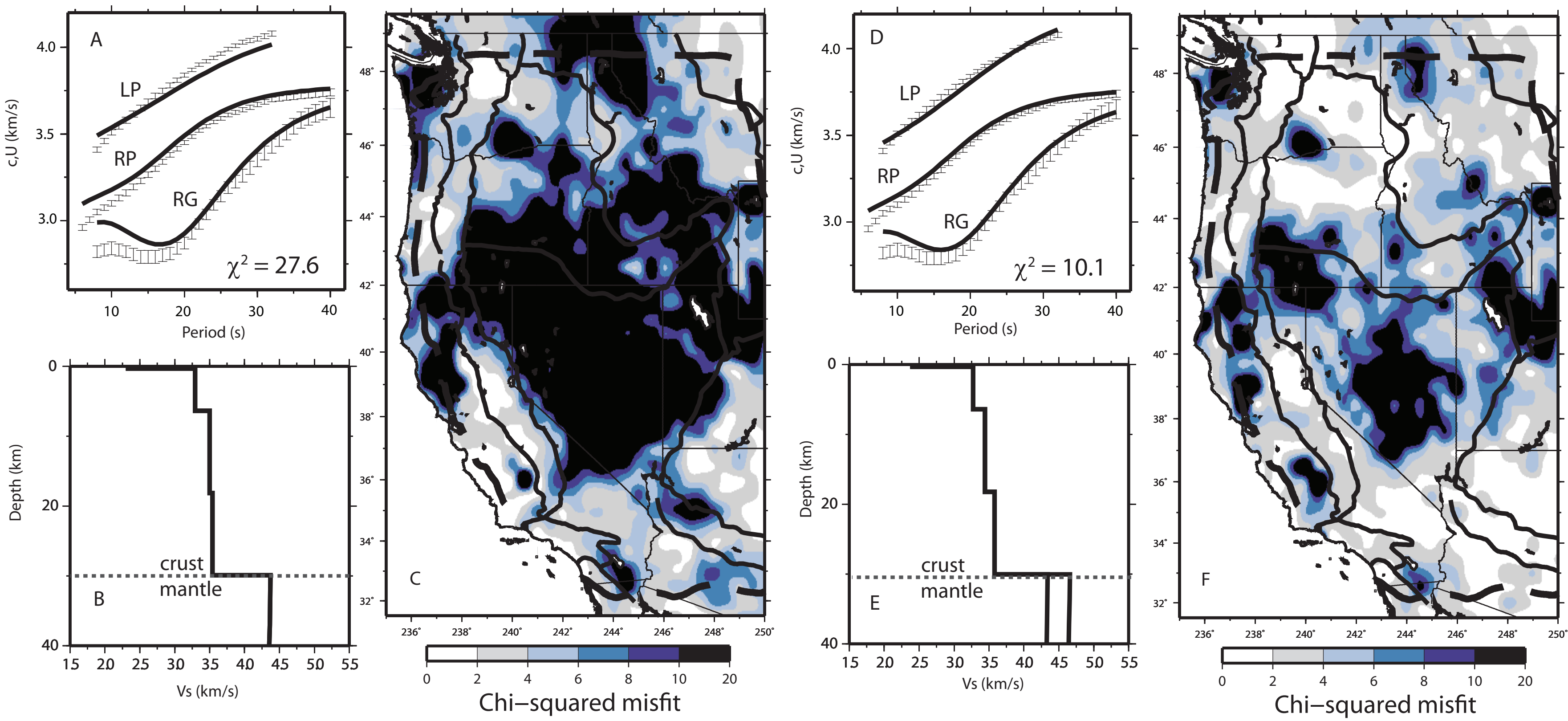

A
LP
RP
RG
$\chi^2 = 27.6$
c,U (km/s)
Period (s)
B
crust
mantle
Depth (km)
Vs (km/s)
C
Chi–squared misfit
D
LP
RP
RG
$\chi^2 = 10.1$
c,U (km/s)
Period (s)
E
crust
mantle
Depth (km)
Vs (km/s)
F
Chi–squared misfit

Figure 2

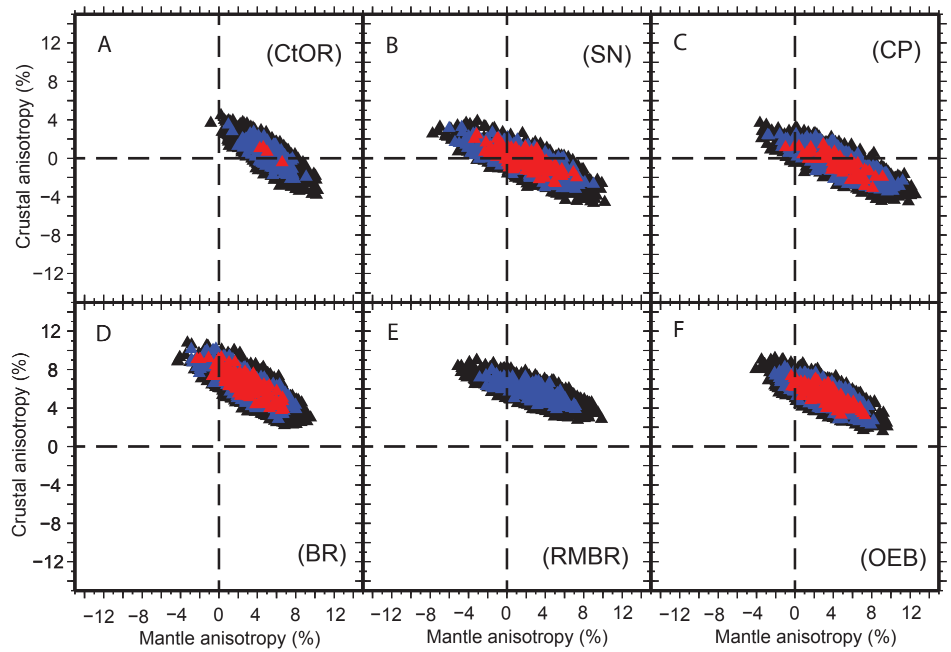
A
(CtOR)
B
(SN)
C
(CP)
D
(BR)
E
(RMBR)
F
(OEB)
Crustal anisotropy (%)
Mantle anisotropy (%)
12
8
4
0
−4
−8
−12

Figure 3

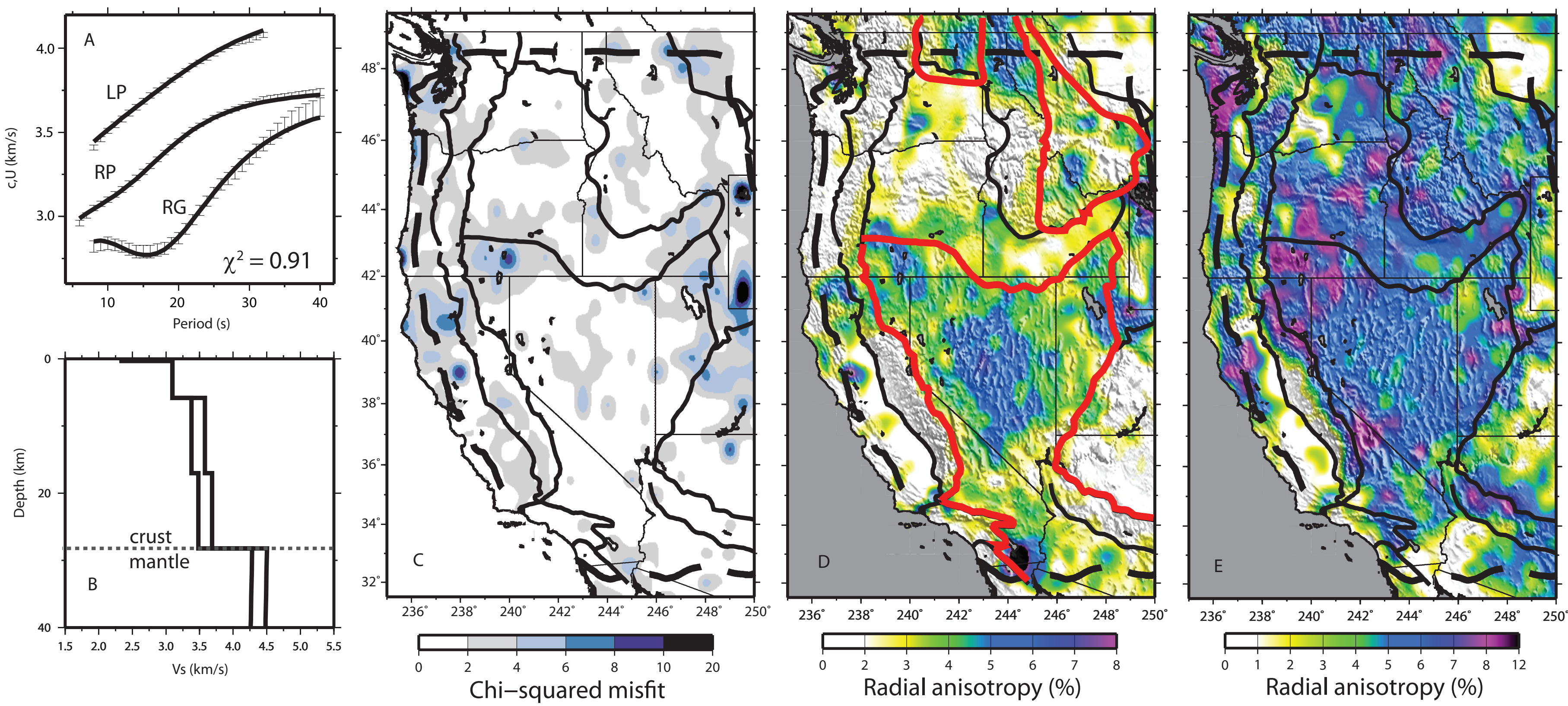

A
LP
RP
RG
$\chi^2 = 0.91$
c,U (km/s)
Period (s)
B
crust
mantle
Depth (km)
Vs (km/s)
C
Chi–squared misfit
D
Radial anisotropy (%)
E
Radial anisotropy (%)

Figure 4

Supporting Online Material

Materials and methods: Error Analysis

Local uncertainties in the dispersion maps are needed for the inversions and to assess resulting data fits to infer causative structures; in particular, the existence of radial anisotropy. Absolute uncertainty estimates for Rayleigh wave phase speed maps derive from the eikonal tomography method of Lin et al. (*1*). Spatially smoothed examples are presented in Figure S2a-d. In general, the uncertainties in these maps grow near the periphery of the seismic array, minimize in the period band between 20 and 30 sec period, and grow at periods longer than 30 sec.

Estimates of the local uncertainty for the Love wave phase speed maps are not yet available and the method is not applicable to group speed maps. To estimate data uncertainties for the Rayleigh wave group and Love wave phase speed maps we scale the Rayeigh wave phase speed uncertainties locally using knowledge of the average relative uncertainty in raw inter-station dispersion measurements. We calculate dispersion measurement uncertainty values following the procedure described by Bensen et al. (*2*). Rayleigh and Love wave dispersion measurements are made sequentially on a set of six-month time series or stacks. The variation in the six-month dispersion measurements compared with the dispersion measurements from the cumulative data stacks is computed for Rayleigh wave group and phase and Love wave phase speed. It is then non-dimensionalized to average relative measurement uncertainty values which are presented in Fig. S2e. Uncertainties in the Rayleigh and Love wave phase speed measurements are nearly identical at all periods, but the Rayleigh wave group speed uncertainties are larger by a period dependent factor of 2–3. Our estimates of the local uncertainty in the dispersion maps result from scaling the Rayleigh wave phase speed maps by the relative measurement error. The spatial average of these maps is shown in Figure S2f. The resulting set of uncertainties in the dispersion maps vary with period, wave type, and location. Uncertainties are lowest in the 20 to 30 sec period band and within the footprint of the USArray Transportable Array.

Supporting references and notes

1. G. D. Bensen et al, *Geophys. J. Int.* **169**, 3 (2007).

2. F. Lin, M. H. Ritzwoller, R. Snieder, *Geophys. J. Int. submitted.*

3. M. P. Barmin, M. H. Ritzwoller, A.L. Levshin, *Pure Appl. Geophys.*, **158**, 8 (2001).

Supplementary Figure Captions

Figure 1. The 16 sec period Rayleigh wave group speed resolution map. Resolution is defined as twice the standard deviation of the 2-D surface Gaussian fit to the resolution map at each point (*3*). Resolution is better than the average inter-station spacing of 70 km within the footprint of the USArray Transportable Array but degrades quickly near the periphery of the array.

Figure 2. Determination of uncertainties in the dispersion maps. (a) - (d) The smoothed Rayleigh wave phase speed uncertainty values from the eikonal tomography method described by Lin et al. (submitted) (*2*) at periods of 8, 16, 24, and 40 sec, respectively. (e) Average relative phase and group speed measurement errors for Rayleigh and Love wave measurements. (f) Spatially averaged Rayleigh phase speed uncertainties provided by eikonal tomography (circles). Spatial average of the Rayleigh wave group (triangles) and Love wave phase (squares) speed uncertainties are estimated by scaling the Rayleigh phase speed uncertainty values by the relative measurement error from (e).

Figure 3. (a) Examples of the set of acceptable models and corresponding local dispersion curves from Inversions I and III in Central Nevada (244.0,40.0). Inversion I results (isotropic model) are plotted in panels (a) and (b) and Inversion III results (crustal and mantle radial anisotropy) are plotted in (c) and (d). In (a) and (c), local Rayleigh wave phase (RP) and group speeds (RG) and Love wave phase speed (LP) and their associated 1-sigma uncertainty values are drawn with black error bars. Dispersion curves for all accepted models are plotted with gray lines. The thick black line denotes the dispersion curve corresponding to the best-fitting model. In (c) and (d), the set of accepted shear-velocity models is drawn in gray, with the best-fitting models plotted in black.

Figure 4. Mantle radial anisotropy from Inversion II in which radial anisotropy is allowed only in the mantle. Major tectonic boundaries are drawn with black lines and the dashed line is the 100 km resolution contour of the 16 sec Rayleigh wave group speed map.

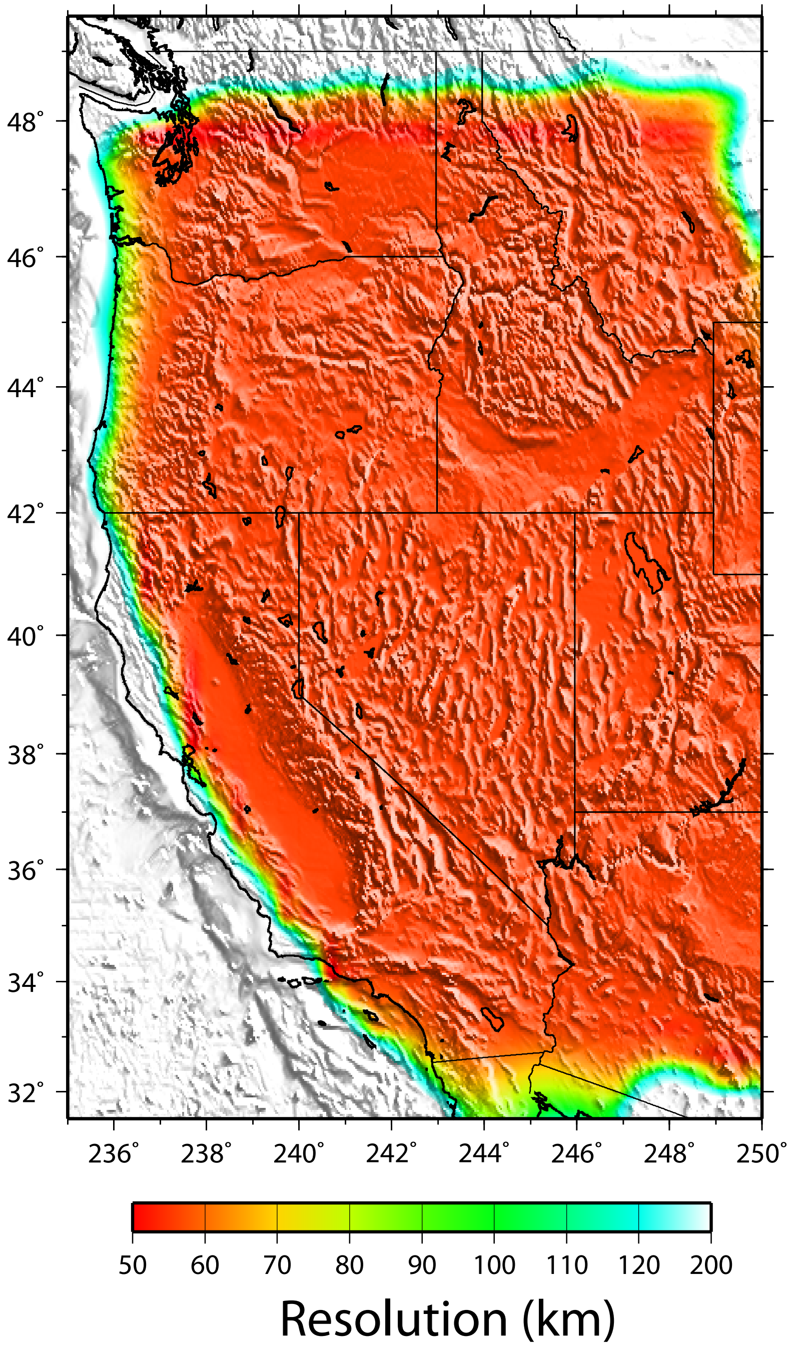

48°
46°
44°
42°
40°
38°
36°
34°
32°
236°
238°
240°
242°
244°
246°
248°
250°
50
60
70
80
90
100
110
120
200
Resolution (km)

Figure S1

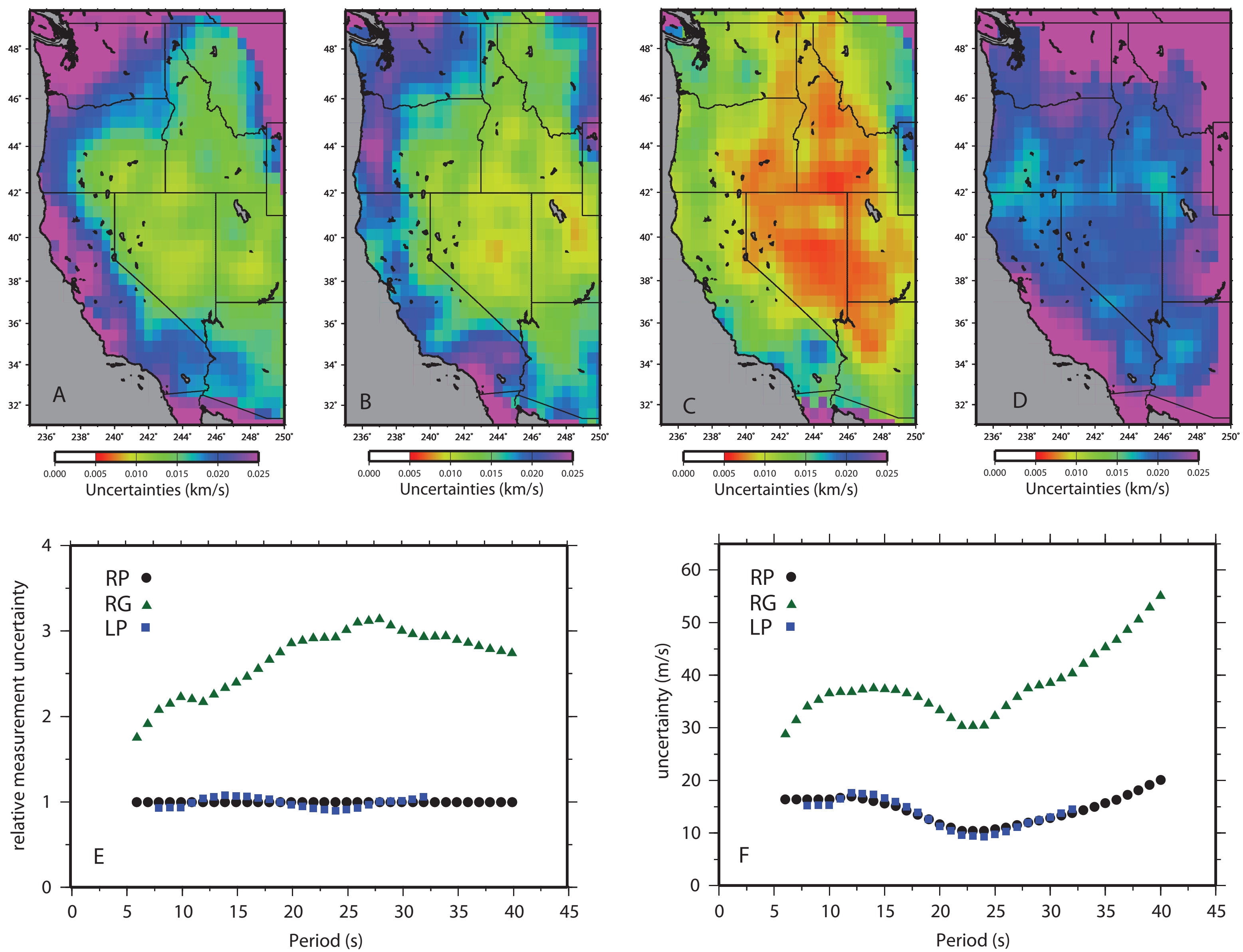
48°
46°
44°
42°
40°
38°
36°
34°
32°
236° 238° 240° 242° 244° 246° 248° 250°
A
B
C
D
0.000 0.005 0.010 0.015 0.020 0.025
Uncertainties (km/s)
RP
RG
LP
relative measurement uncertainty
uncertainty (m/s)
Period (s)
E
F
0 1 2 3 4
0 10 20 30 40 50 60
0 5 10 15 20 25 30 35 40 45

Figure S2

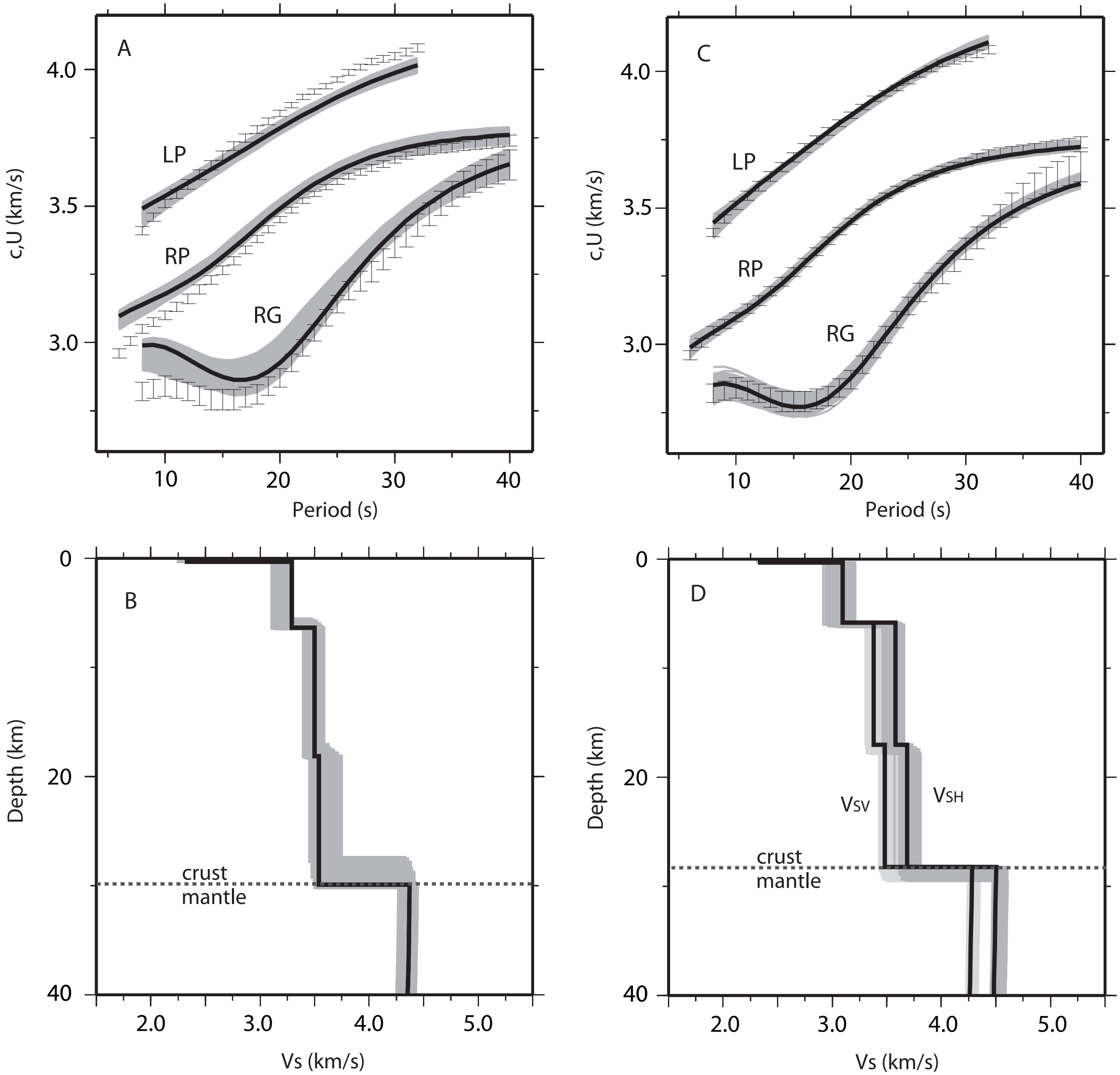

A
LP
RP
RG
4.0
3.5
3.0
c,U (km/s)
10
20
30
40
Period (s)
C
B
0
20
40
Depth (km)
crust
mantle
2.0
3.0
4.0
5.0
Vs (km/s)
D
VSV
VSH

Figure S3

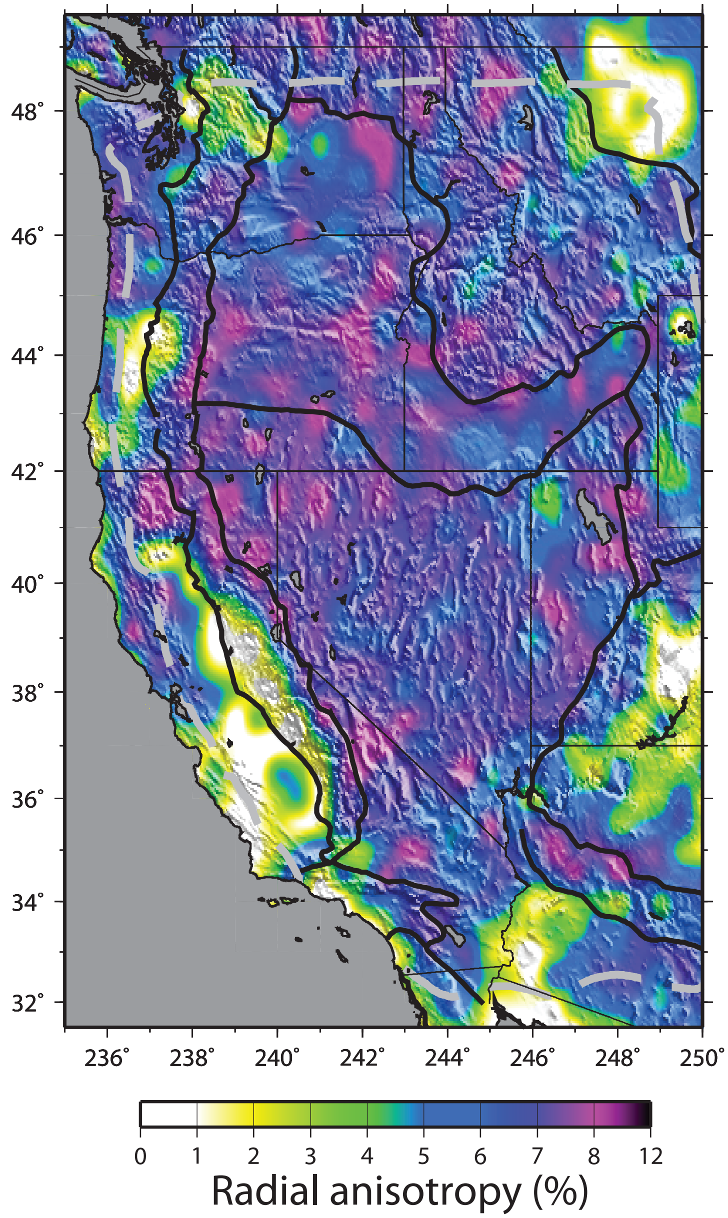
48°
46°
44°
42°
40°
38°
36°
34°
32°
236°
238°
240°
242°
244°
246°
248°
250°
0
1
2
3
4
5
6
7
8
12
Radial anisotropy (%)

Figure S4